Contents lists available at ScienceDirect

Applied Catalysis B: Environmental

Photoactivity of organic xerogels and aerogels in the photodegradation of herbicides from waters

Francisco Orellana-García [a], Miguel A. Álvarez [a], M.V. López-Ramón [a,*],
José Rivera-Utrilla [b], Manuel Sánchez-Polo [b], M. Ángeles Fontecha-Cámara [a]

[a] Department of Inorganic and Organic Chemistry, Faculty of Experimental Science, University of Jaén, 23071 Jaén, Spain
[b] Department of Inorganic Chemistry, Faculty of Science, University of Granada, 18071 Granada, Spain

ARTICLE INFO

ABSTRACT

The objective of this study was to analyze the influence of the presence of organic xerogels and aerogels on the degradation of herbicide amitrole (AMT) by UV radiation. Organic gels were prepared by polycondensation of resorcinol and formaldehyde in water, using Fe, Ni, and Co acetates as catalytic precursors. Materials were characterized by N_2 adsorption at $-196\,^{\circ}C$, pH at the point of zero charge (pH_{pzc}), X-ray diffraction, and X-ray photoemission spectroscopy. The band-gap of these materials was calculated by diffuse reflectance spectra, applying the Kubelka–Munk theory. Results show that the porous texture of gels depends on the salt used, which affects the polymerization rate. Thus, nickel xerogel (X-Ni) has the highest surface area and mesopore volume values. The surface area of Ni aerogel (A-Ni) is four-fold higher than that of its corresponding xerogel, indicating that the drying process also plays a very important role in the textural properties of the material. According to the band-gap values obtained, the gels behave as semiconductor materials, because these values are < 4 eV, ranging between 3.81 eV for X-Na and 3.66 eV for X-Ni. Band-gap values are closely related to the presence of —C=O/—OH groups in the structure of the gels. X-Ni gel has the highest content of —C=O/—OH groups (24.2%). These groups introduce energy bands in the Fermi level, reducing the energy of LUMO–HOMO orbitals. Given the photoactivity of the study materials, AMT removal in the presence of organic xerogels can be attributed to the combination of three factors: direct photolysis, adsorption, and synergic effects. The synergic degradation rate constant (k_{SE}) was found to decrease in the order X-Ni > X-Fe > X-Co > X-Na, passing from 18.7×10^{-3} min^{-1} for X-Ni to 6.0×10^{-3} min^{-1} for X-Na. Results obtained indicate that the positive holes generated in the valence band and electrons, which promote the conduction band, play an essential role in the mechanism by which xerogels enhance AMT photodegradation.

© 2015 Elsevier B.V. All rights reserved.

1. Introduction

An important group in advance oxidation processes (AOPs) is represented by photocatalytic processes in which luminous radiation produces the electronic activation of the semiconductor material that constitutes the catalyst. After irradiation at an appropriate wavelength, this material generates electron/hole pairs that are responsible for the formation of radical species that intervene in the pollutant degradation. These radicals derive both from reduction and oxidation reactions according to their promotion by the electron or by the positive hole generated [1,2].

TiO_2 is one of the materials most widely applied as photocatalysts in water decontamination, both alone and in combination with other materials acting as doping agents and/or material supports [3–6]. Drawbacks in the use of these materials include: their complicated removal from the treated effluent, necessary for their recovery and reutilization; the reduced percentage absorption of solar radiation and the high level of recombination of electron/positive hole pairs. Accordingly, recent studies have centered on photocatalysis processes that reduce these disadvantages. A research line of particular interest in this field has been the preparation of semiconductors with large surface area or their deposition on porous carbon materials [1,7–13].

Carbon xerogels and aerogels are a highly important group of carbon materials [14,15] whose textural and chemical properties and easy preparation have led to numerous applications [16–18]. Carbon gels are obtained by polycondensation reactions

between hydroxyl-benzenes (resorcinol, phenol, catechol, etc.) and aldehydes (formaldehyde, furfural, etc.) in a given solvent (water, methanol, acetone, etc.), followed by a drying stage and subsequent carbonization [17]. A potentially important feature of these materials is that metal-doped aerogel can be readily prepared by adding a soluble metal salt to the initial resorcinol/formaldehyde mixture [14–16]. After gelation, the metal salt is trapped within the gel structure and the metal oxides formed can normally be chelated by functional groups of the polymer matrix. These properties make carbon aerogels very promising materials for enhancing organic pollutant photooxidation processes, because they allow the development of materials with a large surface area and high concentrations of metal oxides of contrasted catalytic activity for the photodegradation of organic compounds on their surface [19].

Amitrole (AMT) is a non-selective herbicide that is sometimes used instead of prohibited herbicides and is extensively employed for weed control in agriculture and along roadsides and railways [20–22]. Due to its high solubility, relatively high AMT levels can be found in surface water and contribute to ground-water contamination *via* leaching [23].

There have been few studies on photocatalytic methods to remove AMT [24,25]. Catastini et al. [21] described the complete removal of AMT from aqueous solutions at pH 3.4, using iron(III) aquo complexes excited by solar and UV radiation to generate HO$^\bullet$ radicals as oxidants. Andersen et al. [26] found that neither ozone nor peroxydisulfate produced any AMT degradation under simulated solar light when used alone and that no increase in AMT *versus* atrazine (ATR) degradation was obtained when used in combination with NF-titania. The authors concluded that this SO$_4^{\bullet-}$ radical-based treatment may be ineffective for the removal of AMT from waters. In a previous study [27] we analyzed the effectiveness of three different systems (UV/H$_2$O$_2$, UV/K$_2$S$_2$O$_8$ and UV/Na$_2$CO$_3$) for AMT photodegradation in different types of water, verifying their high effectiveness, especially that of UV/K$_2$S$_2$O$_8$.

With this background, the main objective of this study was to determine the effectiveness of organic aerogels and xerogels doped with Fe, Co, and Ni in the degradation and removal of AMT in aqueous solution. For this purpose, we prepared and characterized different organic gels doped with Fe, Co, and Ni and analyzed their photoactivity for AMT degradation. We studied the influence of the metal catalyst used in gel polymerization on the textural and chemical properties of these materials and on their photocatalytic capacity. We also analyzed the action mechanism of these gels in AMT photodegradation.

2. Experimental

2.1. Reagents

All chemical reagents used in the present study (amitrole, resorcinol, formaldehyde, sodium carbonate, nickel acetate, iron acetate, cobalt acetate, monobasic sodium phosphate, dibasic sodium phosphate, sodium hydroxide and phosphoric acid) were of high purity analytical grade and supplied by Sigma–Aldrich. All solutions were prepared using ultrapure water obtained with Milli-Q equipment (18.2 MΩ cm).

2.2. Synthesis of organic gels and characterization

Organic aqueous gels were produced from the polycondensation of resorcinol (R) and formaldehyde (F) in water (W), using Fe, Co, or Ni acetates as catalyst precursors [14–16]. The stoichiometric R/F and R/W molar ratios were 0.5 and 0.07, respectively. The amount of acetate added was 1 wt% of the metal in the initial solution. Another organic gel was prepared in the same way

but using carbonate sodium as catalyst. The mixtures were stirred to obtain homogeneous solutions that were cast into glass molds (25 cm length × 0.5 cm internal diameter) and cured for a given time period. The gel rods were then cut into 5-mm pellets and immersed in acetone to remove the water inside the pores. A fraction of this acetone-exchanged sample was dried in supercritical CO$_2$ to form the corresponding organic aerogels. The remaining samples were directly dried at ambient temperature and atmospheric pressure, yielding organic xerogels. Materials are referred to as A or X, denoting the aerogel or xerogel character, respectively, followed by the metal present (Fe, Co, or Ni).

All samples were finally carbonized at 900 °C in a 150 cm^3 min^{-1} N$_2$ flow with a soak time of 5 h and heating rate of 1.5 °C min^{-1}. Carbon aerogels are referred to in the text by adding the letter C to the name of the corresponding aerogel and xerogel.

Samples were characterized by gas adsorption, determination of the pH of the point of zero charge (pH$_{PZC}$), X-ray diffraction (XRD) and X-ray photoelectron emission spectroscopy (XPS). These techniques have been described in detail elsewhere [28].

Aerogel and xerogel samples were texturally characterized using N$_2$ adsorption at −196 °C (Autosorb 1 from Quantachrome). Isotherms were used to determine the BET surface area, S$_{BET}$. Dubinin–Radushkevich and Stoeckli equations were applied to obtain the micropore volume, W$_0$, and mean micropore width, L$_0$. The mesopore volume was obtained as the difference between the amount of N$_2$ adsorbed at a relative pressure of 0.95 and the W$_0$.

The total oxygen content of samples was obtained with an elemental CHNS-O Analyzer Flask (1112 Series) from Thermo Finigan. The pH$_{PZC}$ of samples was determined from potentiometric titrations, as previously reported [29].

XRD patterns were recorded with a PAN analytical Xí'Pert PRO diffractometer using CuKα$_1$ radiation. JCPDS files were searched to assign the different diffraction lines observed. Diffraction patterns were recorded between 2° and 70° (2θ) for 30 min.

XPS measurements were performed with an ESCA 5701 from Physical Electronics equipped with MgKα X-ray source (hυ = 1253.6 eV) and hemispherical electron analyzer. Survey and multi-region spectra were recorded at C$_{1s}$, O$_{1s}$ and Fe$_{2p}$, or Co$_{2p}$, or Ni$_{2p}$, photoelectron peaks.

2.3. Experimental system

AMT degradation experiments were conducted in a UV laboratory reactor system 3 (UV Consulting Peschl). The reactor used was a 1000 mL cylindrical glass contactor equipped with a low-pressure mercury vapor lamp (TNN 15/32, nominal power 15 W) that emitted monochromatic radiation at 254 nm. The rate of energy irradiated by the lamp was determined by actinometry, using a solution of 5 μM ATR as actinometer [30] and obtaining an energy of 1.28 × 10^{-4} Einstein s^{-1} m^{-2} for the lamp.

The superoxide radicals (O$_2^{\bullet-}$) generated were determined by reaction with tetranitromethane (TNM), evaluating the formation of nitroform anions (C(NO$_2$)$_3^-$) [31]. The appropriate amount of TNM was added to the solution irradiated in the presence of 250 mg L^{-1} of gel at an initial concentration of 10^{-4} M, waiting for 20 min to allow the reaction of TNM and O$_2^{\bullet-}$ radicals to take place and then determining the amount of (C[NO$_2$]$_3^-$) generated.

The influence of positive holes (h$_{VB}^+$) on the action mechanism of xerogels was determined by conducting experiments in the presence of ethylenediaminetetraacetic acid (EDTA), which acts as g$^+$ scavenger. Thus, AMT photodegradation kinetics were studied in the presence of gel and EDTA, using initial concentrations in the reactor of 0.30 × 10^{-3} mol L^{-1} AMT, 250 mg L^{-1} gel, and 3 × 10^{-3} mol L^{-1} EDTA.

2.4. Analytical methods

AMT concentrations in solution were determined by reverse-phase high-performance liquid chromatography (HPLC) using a chromatograph (Thermo-Fischer) equipped with UV8000 photo-diode detector. The chromatographic column used was a Hypersil GOLD 250×4.6 mm. The mobile phase was water (pH 6, using phosphate buffer) in isocratic mode and an elution flow rate of $1 \, mL \, min^{-1}$. The injection volume was $20 \, \mu L$ in all samples. The detector wavelength was 202 nm.

The concentration of the nitroform anions $C(NO_2)_3^-$ was determined with a CECIL CE 7200 spectrophotometer at a wavelength of 350 nm. Dissolved oxygen was measured with a DO 6+ portable dissolved oxygen meter.

3. Results and discussion

3.1. Chemical and textural characterization of Fe(II), Co(II), and Ni(II) organic gels

Table 1 lists the textural characteristics of the organic xerogels and aerogels doped with transition metals. The organic xerogels were mainly mesoporous. The presence of metals increased the porosity of the xerogel with respect to the blank (X-Na). X-Ni had the highest S_{BET} ($103 \, m^2 \, g^{-1}$), W_0 ($0.040 \, cm^3 \, g^{-1}$), and V_m ($0.295 \, cm^3 \, g^{-1}$) values. These results suggest that the porous texture of xerogels depends on the nature of the metal salt, which affects the rate of polymerization that leads to the gel formation [32]. The pH of the initial mixture that gave rise to samples X-Ni, X-Co, and X-Fe was 6.2, 6.1, and 4.3, respectively. The differences in pH among the initial samples may explain the varied textural characteristics of the xerogels obtained. These results indicate that Ni and Co acetates are superior polymerization catalysts [32,33]. The cations of the acetates used, dissolved in water, formed the corresponding hexa-aquo complexes. The ionic radius of the hydrated cation was 2.43 Å for $Na(H_2O)_6^+$, 2.12 Å for $Fe(H_2O)_6^{2+}$, 2.08 Å for $Co(H_2O)_6^{2+}$, and 2.05 Å for $Ni(H_2O)_6^{2+}$. The larger size of the cation increased the gelation time, because weaker interactions were established between the particles of the polymer formed and the cations. Longer gelation and mobility time favors the overlapping of primary hydrogel particles and the formation of particle clusters. A greater overlapping also produces a larger volume and size of the holes between the particles, resulting in an increased pore size [34]. The results in Table 1 show that mean micropore size, (L_0), determined with N_2 augmented in the same order as the ionic radius of the hydrated cation: X-Ni < X-Co < X-Fe < X-Na. However, the samples had a larger number of micropores and mesopores with lower cation radius; hence, their micro- and mesopore volumes and consequently their surface area increased in the order X-Na < X-Fe < X-Co < X-Ni (Table 1). Similar results were previously obtained using different Cr, Mo, and W salts as polymerization catalysts in aerogel synthesis [16]. As shown in Table 1, Fe and Ni xerogels were less porous than the corresponding aerogels with the same baseline composition, as reported by other authors [35]. These results indicate that the drying method has a decisive influence on the dried polymer networks [36]. The organic aerogels had W_0 and V_m values, respectively, of 0.173 and $0.678 \, cm^3 \, g^{-1}$ for A-Fe and of 0.185 and $0.717 \, cm^3 \, g^{-1}$ for A-Ni. These values were much higher than those of their respective organic xerogels, which is related to the different drying procedure used. Thus, drying with supercritical CO_2 yields organic gels with larger surface area and micro- and mesopore volumes because it minimizes surface tension on the pores during solvent removal, reducing their collapse and preserving the porous texture created during gel synthesis.

Fe and Ni xerogel and aerogel samples underwent a process of carbonization in nitrogen atmosphere at 900 °C for 5 h. Table 1 shows that the carbonization process increased the microporosity of samples, augmenting their surface area. However, in the case of the aerogels, carbonization considerably reduced their mesoporosity.

As shown in Table 2, the pH_{PZC} value ranged between 3.1 and 3.6 for both xerogels and aerogels, demonstrating their acid nature. The surface basicity of the samples markedly increased after carbonization, with a pH_{PZC} value of around 7. This was mainly due to the removal of oxygenated surface groups at the high temperatures used during carbonization [19,37], as indicated by the low percentage oxygen values for the carbonized samples (Table 2).

Table 2 also displays the results of the elemental analysis of the prepared gels, showing the elevated percentage oxygen values of both xerogels and aerogels. These findings indicate the high concentration in these materials of oxygenated groups; which were mostly eliminated during the carbonization, as noted above. We highlight the low ash content of these materials (Table 2). Fig. 1a depicts the X-ray diffractograms of the organic xerogels. As observed, there was no diffraction peak corresponding to the metal present, indicating its wide dispersion on the xerogel surface. Fig. 1 also depicts the X-ray diffractograms of the gels containing iron (Fig. 1b) and nickel (Fig. 1c). As observed in Fig. 1b, only carbonized samples showed diffraction peaks. In the case of carbonized samples XC-Fe and AC-Fe, diffraction peaks were observed at 35.6° and 43.3°, respectively, and assigned to Fe_3O_4 (JCPDS 88-0866) and γ-Fe_2O_3 (JCPDS 39-1346). The peak centered at 44.7° (XC-Fe) is characteristic of metallic Fe (JCPDS 306-0696). Gels A-Fe and X-Fe showed no diffraction peaks corresponding to iron oxides.

Fig. 1c depicts the diffractograms of gels containing nickel. As in the case of the iron gels, diffraction peaks corresponding to Ni species were only detected in the carbonized samples. Thus, samples AC-Ni and XC-Ni showed diffraction peaks at 44.6° and 51.9°, respectively, indicating the presence of metallic Ni (JCPDS 04-0850).

The nature of the surface oxygen groups was determined by deconvolution of the XPS spectra of O_{1s} for each sample (Table 3). The surface oxygen was mainly distributed as −C=O/−OH (oxygen of the carbonyl group present in lactones, anhydrides, and oxygen atoms of hydroxyl groups) and −C−O−C− (oxygen atom in lactones and anhydride). The proportion of −C−O−C− groups was higher than that of -C=O/-OH groups in all samples. The X-Ni sample showed the highest percentage of −C=O/−OH groups (24.2%) among all study samples.

3.2. Determination of electrical properties

The electrical properties of the studied materials were analyzed by obtaining the diffuse reflectance spectra (DRS), allowing determination of the band-gap or forbidden band energy [38–40]. The analysis was based on the Kubelka-Munk theory, which assumes that the radiation reaching a dispersing medium simultaneously undergoes processes of absorption and dispersion. Hence, the reflected radiation can be defined as a function of absorption (k) and dispersion (s) constants, as shown in Eq. (1):

$$F(R) = \frac{[1 - R_\infty]}{2R_\infty} = \frac{k}{s} \tag{1}$$

where $F(R)$ is the Kubelka–Munk function, corresponding to the absorbance, R_∞ is the absorbance of a sample with infinite width with respect to a standard (barium sulfate) for each measured wavelength, k is the absorption coefficient, and s is the dispersion coefficient. Assuming a constant material dispersion in the studied

Table 1
Textural characteristics of organic xerogels and aerogels.

Sample	S_{BET}[a] ($m^2\,g^{-1}$)	W_0[b] ($cm^3\,g^{-1}$)	V_m[c] ($cm^3\,g^{-1}$)	E_0[d] ($kJ\,mol^{-1}$)	L_0[e] (nm)
X-Na	2	0.002	0.030	6.7	3.60
X-Co	68	0.031	0.194	10.3	2.34
X-Fe	27	0.012	0.089	8.8	2.73
X-Ni	103	0.040	0.295	12.1	1.99
A-Fe	388	0.173	0.678	9.8	2.44
A-Ni	407	0.185	0.717	12.4	1.93
XC-Fe	338	0.134	0.225	21.5	1.07
XC-Ni	382	0.144	0.230	20.7	1.16
AC-Fe	568	0.221	0.396	21.1	1.11
AC-Ni	637	0.249	0.371	23.5	0.89

[a] Surface area determined by N_2 adsorption isotherms at $-196\,°C$.
[b] Micropore volume from DR equation applied to N_2 adsorption isotherms at $-196\,°C$.
[c] Mesopore volume from N_2 adsorption isotherms at $-196\,°C$.
[d] Characteristic adsorption energy from DR equation applied to N_2 adsorption isotherms at $-196\,°C$.
[e] Mean micropore width from DR equation applied to N_2 adsorption isotherms at $-196\,°C$.

Table 2
Gel characterization. pH_{PZC}, E_g, ash content, and elemental analysis.

Sample	pH_{PZC}	E_g (eV)	Ash (%)	Elemental analysis (%)		
				C	H	O
X-Na	3.6	3.81	0.1	59.2	3.3	37.4
X-Co	3.6	3.78	0.7	58.4	3.3	37.6
X-Fe	3.5	3.74	1.1	57.6	3.2	38.1
X-Ni	3.4	3.66	1.0	63.5	3.5	32.0
XC-Fe	7.3	4.35	2.1	93.8	0.2	3.9
XC-Ni	7.0	4.16	2.0	89.6	0.5	7.9
A-Fe	3.1	3.75	0.5	59.8	3.3	36.4
A-Ni	3.6	3.69	0.5	61.6	4.0	33.9
AC-Fe	7.1	4.47	0.8	89.1	0.4	9.7
AC-Ni	6.9	4.44	1.7	89.5	0.3	8.5

wavelength range, Eq. (1) depends on the absorption coefficient alone, transforming Eq. (1) into Eq. (2):

$$F(R) = \frac{(1 - R_\infty)^2}{2R_\infty} = \alpha \tag{2}$$

It has been demonstrated in different transition mechanisms that the energy of incident photons and the band-gap (E_g) of the material are related in the absorption process as follows (Eq. (3)):

$$\alpha \times h\nu = C\left(h\nu - E_g\right)^n \tag{3}$$

where α is the linear absorption coefficient of the material, h is Planck's constant ($4.136 \times 10^{-15}\,eV\,s^{-1}$), C is the model adjustment constant, $h\nu$ is the photon energy (eV), E_g is the band-gap energy (eV), and n is the constant for the type of optical transition, with values of $n = 2$ for permitted indirect transitions, $n = 3$ for forbidden indirect transitions, $n = 1/2$ for permitted direct transitions, and $n = 3/2$ for forbidden direct transitions. Eq. (4) is then obtained by substituting Eq. (2) in Eq. (3):

$$(F(R) \times h\nu)^{\frac{1}{n}} = C\left(h\nu - E_g\right) \tag{4}$$

Based on Eq. (4), it was possible to represent $(F(R) \times h\nu)^{1/n}$ versus $h\nu$ and the E_g could be obtained. A value of $n = 1/2$ was considered for permitted direct transitions, as suggested by other authors [41]. The adjustment error was minimized by conducting double linear fitting and obtaining the E_g value as the cutoff point of both lines [42]. As an example, Fig. SM 1 depicts the determination of E_g for nickel aerogel (A-Ni).

Table 2 exhibits the results obtained for the study samples. According to the E_g values obtained, which were <4 eV in all cases, the organic gels (xerogels and aerogels) behaved as semiconductor materials and therefore as photoactive materials in the presence of UV radiation. Interestingly, the band-gap value of each aerogel was very close to that of the corresponding xerogel. In xerogels,

the band-gap ranged between 3.66 eV for X-Ni and 3.81 eV for X-Na. Band-gap values decreased in the order X-Na > X-Co > X-Fe > X-Ni and depended on the surface and structural properties of the semiconductors. No relationship was found between the band-gap values and textural characteristics of the xerogels (Table 1). However, their band-gap values were found to be related to their chemical properties; as observed in Table 3, the order of their content of −C=O/−OH groups was the opposite of the order of their band-gap values, with X-Ni having the highest content (24.2 %). Milowska et al. [43] reported that the presence of −COOH and −OH groups can alter the electrical properties of materials, introducing "impurity" bands around Fermi level and reducing the energy between LUMO and HOMO orbitals. The presence of oxygen atoms also facilitates the promotion of a larger number of electrons to the conduction band through the formation of carbon-oxygen bonds and of new molecular orbitals in the system [2,44].

The crystallinity of a material plays an important role in its photocatalytic activity, besides its specific surface area. Sifontes et al. [45] evaluated the effect of carbonization temperature on the band-gap of various synthesized CeO_2 samples, finding that an increase in temperature from 350 to 960 °C increased the band-gap from 3.02 to 3.41 eV, augmenting the crystal size.

The presence of 3d transition metals (Fe, Co, and Ni) in organic xerogels reduced the band-gap with respect to X-Na xerogel, as shown in Table 2. This is due to delocalized states in transition metals, which contribute to the formation of new energy bands by hybridization with 2p states of oxygen. These energy bands constitute new energy levels in the band-gap or form hybrid states with the valence or conduction layer, contributing to band-gap reduction and favoring the formation of photogenerated electron-positive hole pairs and photocatalysis [46]. Although new energy states are formed between valence and conduction bands in all three studied metals, hybrid states also arise in the valence layer in the case of
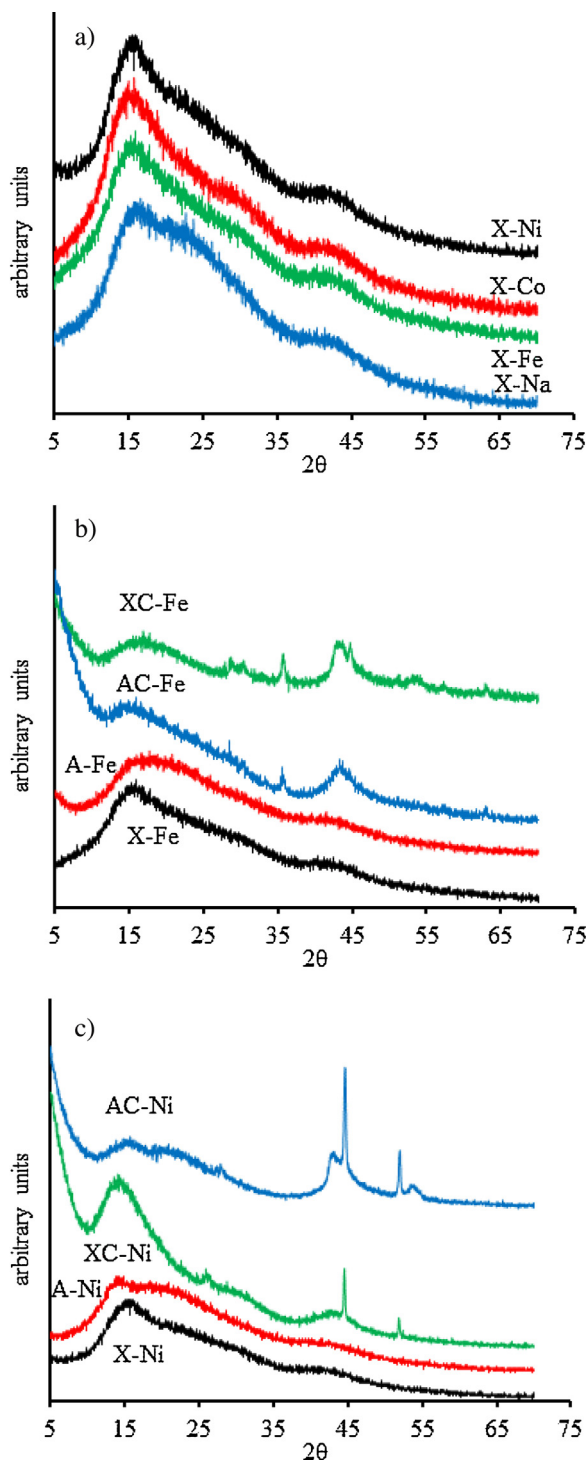
Fig. 1. (a) XRD patterns of organic xerogels. XRD patterns of metal-doped organic gels and their carbonized derivatives. (b) Fe; (c) Ni.
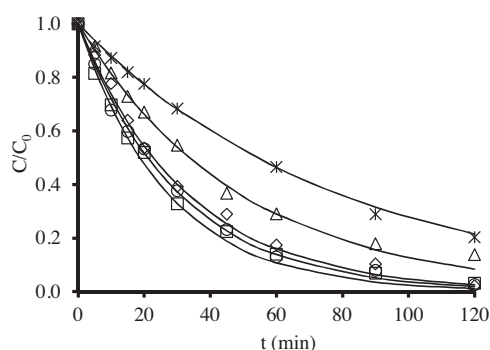

Fig. 2. Removal kinetics of AMT at 25 °C with the UV/organic xerogel system as a function of treatment time. [AMT]$_0$ = 0.30 mM, T = 25 °C. ($\ast$) Direct photolysis; ($\triangle$) X-Na; ($\diamond$) X-Co; (O) X-Fe; ($\square$) X-Ni.

Table 3
Deconvolution of O1s XPS spectra of the organic and carbon gel samples (%).

Sample	—C=O/—OH 532.2 ± 0.2 eV	—C—O—C— 533.1 ± 0.2 eV	H$_2$O 535.1 ± 0.4 eV
X-Na	16.6	65.3	18.1
X-Co	18.0	66.2	15.8
X-Fe	20.4	60.1	19.5
X-Ni	24.2 (28.4[a], 29.6[b])	51.2(49.2[a], 51.9[b])	24.6(22.4[a], 18.5[b])
XC-Fe	7.9	38.0	54.1
XC-Ni	9.6	36.6	53.8
A-Fe	19.9	51.1	29.0
A-Ni	22.6	46.4	31.0
AC-Fe	10.3	30.8	58.9
AC-Ni	11.7	33.7	54.6

[a] At 45 min irradiation.
[b] At 90 min irradiation.

3.3. AMT photodegradation by UV radiation in the presence of organic gels

Fig. 2 depicts AMT photodegradation kinetics by UV radiation and by the simultaneous use of UV radiation and organic xerogels. There was a marked increase in the removal rate when the process was conducted in the presence of organic xerogels doped with transition metals. Based on the photodegradation kinetics obtained, we calculated the total removal rate constants of AMT removal ($k_{UV/GEL}$) (Table 4). The rate constant $k_{UV/GEL}$ was obtained by using first order kinetics. The time to degrade 90% AMT decreased with the use of transition metal-doped xerogels, obtaining the shortest time, 62.1 min, with the X-Ni sample. The total removal rate constant of AMT confirmed the increased AMT photodegradation rate in the presence of xerogels (Fig. 2).

AMT photooxidation by the simultaneous use of UV radiation and organic gels is a complex process. AMT is degraded not only by the hydroxyl and superoxide radicals generated in the interaction of UV radiation with organic gel but also by direct AMT photolysis and adsorption on the organic gel in the medium. The reduction in AMT concentration can therefore be described as the result of three processes in combination: (a) direct photolysis; (b) adsorption, and (c) the synergic effect produced by the presence of the gel. This synergic effect has a positive sign if it favors AMT degradation, is equal to zero if it does not affect the process, and has a negative sign if it inhibits AMT degradation. Accordingly, AMT removal in the presence of gel can be mathematically described by the following equation:

$$-V_{UV/GEL} = -\frac{[dAMT]}{dt} = -(V_{UV} + V_{ADS} + V_{SE})$$
$$= -(k_{UV} + k_{ADS} + k_{SE}) \times [AMT] \tag{5}$$

Ni, increasing the electron density, decreasing the band-gap of the material, and favoring the promotion of electrons to higher energy bands [47].

As observed in Table 2, the band-gap of gels markedly increases after carbonization, reaching values superior to those corresponding to a semiconductor material (>4 eV). This rise in the forbidden energy band is due to the removal of oxygenated groups from gels by carbonization (Table 2), which reduces the number of molecular orbitals and therefore augments the energy difference between LUMO and HOMO orbitals.

where k_{UV} is the AMT removal rate constant due to direct photolysis, k_{ADS} is the rate constant of the adsorption process, and k_{SE} expresses the influence on $k_{UV/GEL}$ of the presence of gel in the medium (synergic effect). Calculation of the k_{SE} value and its sign therefore requires separate determinations of the contribution of direct photolysis and adsorption to the global removal process.

The percentage removal due to the synergic effect of the gels was calculated by subtracting adsorptive and photolytic contributions from the total percentage removal in the UV/GEL system (Eq. (6)). Table 4 shows the results obtained at 45 min of treatment.

$$\%SE_{UV/GEL} = \%D_{UV/GEL} - \%D_{UV} - \%A_{GEL} \tag{6}$$

where $\% SE_{UV/GEL}$ is the percentage AMT removal due to the synergic effect produced by the presence of the gel during exposure to UV radiation, $\%D_{UV/GEL}$ is the total AMT degradation in the UV/GEL photocatalytic process, $\%D_{UV}$ is the percentage AMT degradation by direct photolysis, and $\%A_{GEL}$ is the percentage AMT removed by adsorption on organic gel.

The results in Table 4 indicate that $k_{UV/GEL}$ decreased in the order: X-Ni > X-Fe > X-Co > X-Na, passing from 37.1×10^{-3} min^{-1} (X-Ni) to 20.6×10^{-3} min^{-1} (X-Na). The percentage removal also decreased in the same order, reaching 77.6% for Ni xerogel and 63.3% for Na xerogel at 45 min (Table 4).

As observed, the order of variation of the k_{SE} rate constant was the same as that of the $k_{UV/GEL}$ constant. Likewise, the percentage removal of X-Ni was higher, given the synergic effect (24.4% at 45 min) and the lower adsorptive contribution to the AMT removal process. The lowest percentage removal and smallest adsorptive and synergic contributions were obtained with xerogel X-Na.

This synergic effect can also be quantified by calculating synergic factor R [48,49], i.e., the ratio between the photodegradation kinetics constant in the presence of the gel and the sum of photolysis and adsorption constants according to Eq. (7):

$$R = \frac{k_{UV/gel}}{k_{UV} + k_{ads}} \tag{7}$$

$R > 1$ indicates a synergic effect, while $R < 1$ indicates an inhibition of pollutant photodegradation in the presence of the material.

Among the organic xerogels studied, the synergic factor was higher with X-Ni (2.0) than with Ni and Fe aerogels. The synergic effect virtually disappeared in carbonized samples, which had synergic factor values ≤ 1.0 (Table 4).

Fig. 3 depicts the time course of the synergic contribution to global AMT removal as a function of irradiation time. As observed, the synergic contribution for xerogels increased up to a maximum at 45 min irradiation and then decreased to virtually zero at 120 min. The synergic effect was evaluated in the absence of the adsorption process by conducting experiments in which the organic xerogel was saturated with AMT (Fig. SM 2). The Fe xerogel showed $k_{SE} = 14.8 \times 10^{-3}$ min^{-1}, indicating that the synergic effect
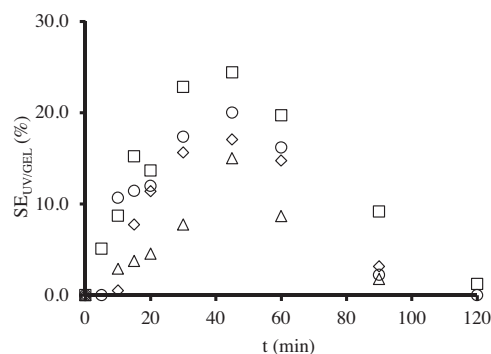

Fig. 3. Percentage AMT removal by the synergic effect produced by the presence of gel during exposure to UV radiation as a function of treatment time. $[AMT]_0 = 0.30$ mM, $T = 25$ °C. ($\triangle$) X-Na; ($\diamond$) X-Co; (O) X-Fe; ($\square$) X-Ni.

was maintained in the saturated xerogel. The global percentage AMT degradation was 70.8% in the UV/GEL photocatalytic process ($D_{UV/GEL}$) at 45 min of treatment, with 30.3% being due to the synergic effect produced by the presence of gel during UV radiation exposure ($\%SE_{UV/GEL}$).

The above variables were all markedly reduced with the use of aerogels rather than xerogels. As shown in Table 4 and Fig. SM 3, the use of aerogels (A-Ni or A-Fe) instead of the corresponding xerogels produced a mean reduction of 6.5×10^{-3} min^{-1} in the total degradation rate constant and a decrease in synergic effect values. The percentage degradation was also lower (Table 4), indicating that the drying time in the synthesis process affects the photocatalytic activity of the material [36].

As observed in Table 2, band-gap values for non-carbonized gels were <4 eV; therefore, they behaved as photoactive materials in the presence of UV radiation. Lower E_g values corresponded to higher $k_{UV/GEL}$ and k_{SE} values (Table 4). X-Ni showed the lowest E_g (3.66 eV) and the highest synergic rate (18.7×10^{-3} min^{-1}) and synergic percentage degradation (24.4%). The E_g values of carbonized gels were >4 eV; therefore, these materials were not photoactive and the synergic component was virtually null in the AMT photodegradation process (Table 4).

3.4. Determination of the reaction mechanism

Velo-García et al. [2] proposed a mechanism to explain the photoactivity of activated carbons. The photons from UV light reach the materials and generate electron-positive hole pairs through their irradiation with sufficient energy to promote electrons from the valence band to the conduction band. The photogenerated electrons can spread through graphene layers and reach molecules of the absorbed compound and oxygen molecules. In the latter case, these electrons can reduce the adsorbed O_2 to form the superoxide

Table 4
Reaction rate constants and synergic contribution to AMT degradation by UV/organic gels and carbonized gels system. $[AMT]_0 = 0.30$ mM, [Catalyst] = 250 mg/L, pH = 7.

Sample	$t_{90\%}$ min	$k_{UV/GEL}$ 10^3 min^{-1}	k_{ADS} 10^3 min^{-1}	k_{SE} 10^3 min^{-1}	R	$D_{UV/GEL}$ (%, 45 min)	A_{GEL} (%, 45 min)	$SE_{UV/GEL}$ (%, 45 min)
X-Na	111.7	20.6	1.8	6.0	1.4	63.3	7.8	15.0
X-Co	75.4	30.6	5.9	11.9	1.6	71.1	13.6	17.1
X-Fe	70.0	32.9	6.0	14.1	1.8	76.8	16.3	20.0
X-Ni	62.1	37.1	5.6	18.7	2.0	77.6	12.7	24.4
A-Fe	86.7	26.3	8.7	4.8	1.2	69.1	16.2	12.4
A-Ni	75.0	30.7	8.0	9.9	1.5	75.2	12.3	22.5
XC-Ni	77.4	29.7	13.2	3.7	1.1	70.7	26.2	4.1
AC-Ni	99.4	23.2	13.4	–	0.9	64.3	24.0	-
XC-Fe	97.2	24.0	11.1	–	1.0	69.5	27.6	1.4
AC-Fe	106.2	21.7	12.7	–	0.9	61.2	19.8	0.9

$k_{UV} = 12.8 \times 10^{-3}$ min^{-1}.
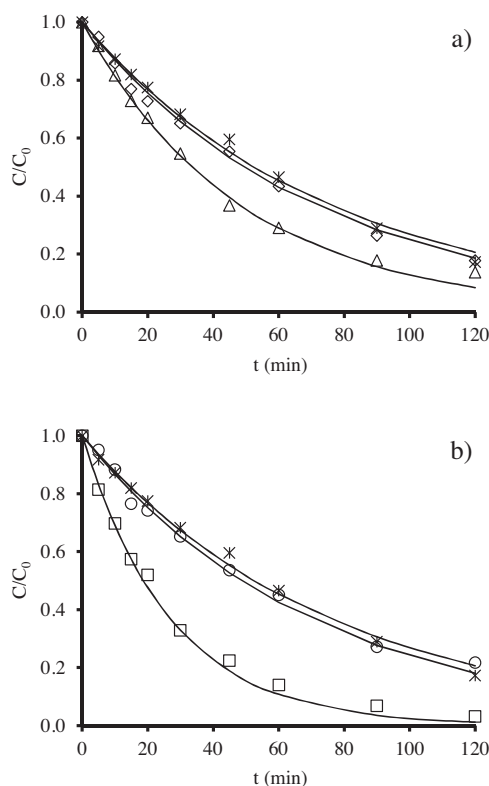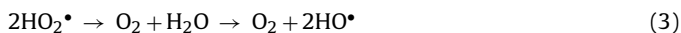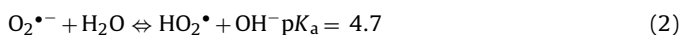$D_{UV} = 40.5$ (%, 45 min).

Fig. 4. AMT removal kinetics at 25 °C with the UV/organic xerogel system as a function of treatment time in presence and absence of EDTA. $[AMT]_0 = 0.30$ mM, $T = 25$ °C. (a) ($\ast$) Direct photolysis; ($\triangle$) X-Na; ($\diamond$) X-Na+EDTA. b) ($\square$) X-Ni; (O) X-Ni+EDTA.

radical (O_2^-), which may react with the water molecule, triggering the formation of more oxidizing radical species [50] that will interact with the compound, contributing to its degradation (Reactions (1)–(3)).

$$e^-_{CB} + O_2 \rightarrow O_2^{\bullet -} \tag{1}$$

$$O_2^{\bullet -} + H_2O \Leftrightarrow HO_2^\bullet + OH^- \, pK_a = 4.7 \tag{2}$$

$$2HO_2^\bullet \rightarrow O_2 + H_2O \rightarrow O_2 + 2HO^\bullet \tag{3}$$

The positive holes (h^+_{VB}) are directly responsible for the generation of hydroxyl radicals by capturing the water molecule (Reaction (4)).

$$h^+_{VB} + H_2O \rightarrow HO^\bullet + H^+ \tag{4}$$

The reaction mechanism was first investigated by determining the influence of positive holes using AMT photodegradation experiments in the absence and presence of EDTA. Photodegradation kinetics were analyzed and the effectiveness of photocatalysts was evaluated according to the levels of AMT removal at different irradiation times. Fig. 4 depicts, as an example, the results obtained for UV/X-Na and UV/X-Ni systems. As observed in both cases, addition of EDTA to the UV/xerogel system reduced the AMT photodegradation rate. In the case of X-Ni, the total removal rate constant decreased from 37.1×10^{-3} min^{-1} to 14.3×10^{-3} min^{-1}, a similar value to that obtained with direct photolysis, 12.8×10^{-3} min^{-1}. These results corroborate that the xerogels act as photoactive materials and that the suppression of positive holes totally inhibits their photocatalytic role in AMT degradation.

Fig. 5 depicts the results obtained in the presence of tetranitromethane (TNM), showing that the presence of the two organic xerogels during photodegradation increased the concentration of superoxide radicals, the concentration of superoxide radicals generated was superior with X-Ni than with X-Na. The maximum O_2^-
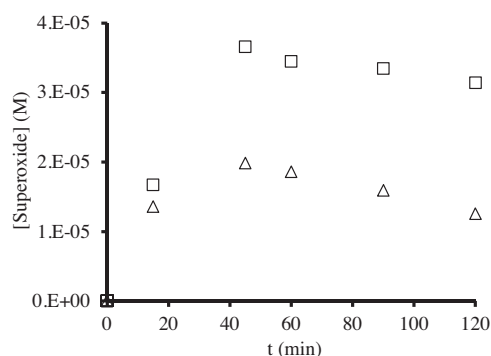

Fig. 5. Formation of superoxide radicals. ($\triangle$) X-Na; ($\square$) X-Ni.
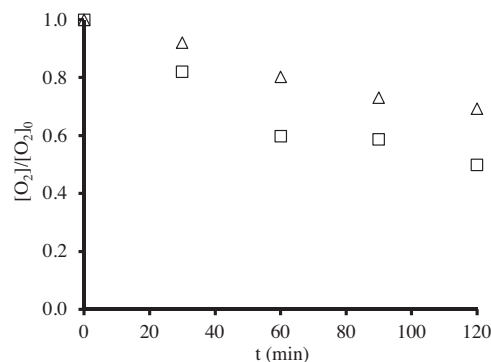

Fig. 6. Time course of dissolved oxygen in the UV/xerogel system. ($\triangle$) X-Na; ($\square$) X-Ni.

generation was reached at 45 min of irradiation, when the maximum photocatalytic activity was observed (Fig. 3), evidencing that the generation of superoxide radicals positively contributed to AMT photodegradation. This was confirmed by conducting experiments to determine the time course of dissolved oxygen in the solution. Fig. 6 depicts the results obtained, showing that longer irradiation times, regardless of the sample considered, progressively reduced the oxygen concentration, corroborating the reaction mechanism by which superoxide radicals are formed (Fig. 7).

In order to determine the surface chemistry transformation of xerogels during irradiation, XPS analyses were conducted on xerogel samples subjected to UV radiation for different times (Table 3). We highlight that a small fraction of oxygenated groups present on the xerogel surface transformed into other groups during irradiation. For example, the results for X-Ni in Table 3 show a slight increase in the percentage of oxygen that forms part of the −C=O/−OH groups at 45 min irradiation, passing from 24.2 to 28.4%, a decrease of 2% in the percentage of oxygen that forms −C−O−C− groups; and ≈2% reduction in the percentage that forms the H_2O molecule. At the longer irradiation time of 90 min, the percentage of the oxygen that forms part of the −C=O/−OH groups continued rising and that corresponding to the water molecules continued decreasing. These variations in the percentage oxygen of the gels indicate slight changes on their surface with irradiation. These modifications may be due to the oxidation of these oxygenated groups by the positive holes or their reduction by the electrons generated (Fig. 7). The fact that the global balance of oxygenated groups remained constant during irradiation suggests that the carbon matrix of xerogels was not attacked by the oxidizing oxygenated species, mainly hydroxyl radicals, which were formed during irradiation (Fig. 7).
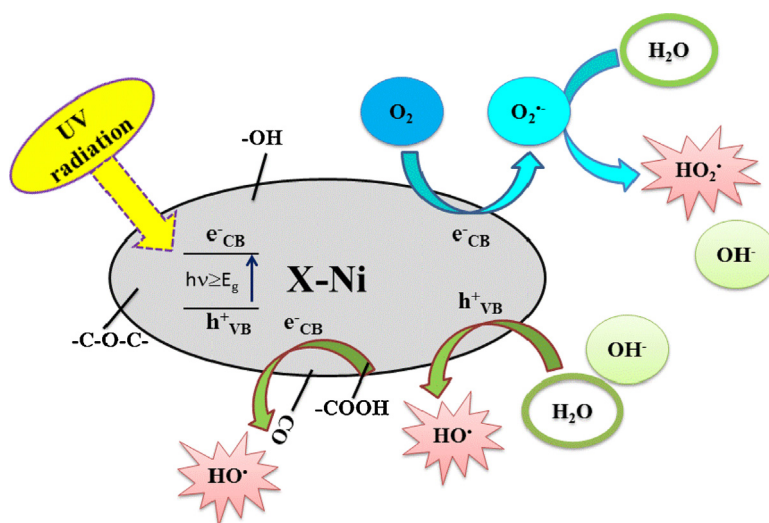
Fig. 7. Mechanism proposed for the action of organic gels as photocatalysts.

5. Conclusions

The porous texture of xerogels depends on the nature of the metal salt, which affects the polymerization rate that leads to the gel formation, with Ni and Co acetates being the best polymerization catalysts.

The mean micropore size of xerogels increases in the same order as the ion radius of the hydrated cation: X-Ni < X-Co < X-Fe < X-Na; however, the number of micropores and mesopores increases with the reduction in cation radius. Hence, their micro- and mesopore volumes and, consequently, their surface area, increase in the order X-Na < X-Fe < X-Co < X-Ni. Carbonization increases the microporosity of samples, augmenting their surface area.

In non-carbonized gels, the band-gap ranges between 3.66 eV for X-Ni and 3.81 eV for X-Na and is related to the chemical properties of these materials. Higher concentrations of —C=O/—OH groups increases the number of bands at Fermi level, which reduces LUMO–HOMO energy and decreases the band-gap energy. Carbonization augments the band-gap of the material to >4 eV through the removal of numerous surface oxygen groups.

The reduction in AMT concentration during irradiation is attributable to the combination of adsorption, direct photolysis, and gel-induced synergic effect. The synergic rate constant decreases in the order: X-Ni > X-Fe > X-Co > X-Na. These results are related to the differences in band-gap energy, which increase in the reverse order.

The presence of xerogels during AMT photodegradation promotes the generation of superoxide and hydroxyl radicals through the photogeneration of electron-positive hole pairs. These pairs can also oxidize and reduce part of the oxygenated groups present on the surface of the xerogels.

Acknowledgements

Appendix A. Supplementary data

Supplementary data associated with this article can be found, in the online version, at http://dx.doi.org/10.1016/j.apcatb.2015.07.044

References

[1] J. Rivera-Utrilla, M. Sánchez-Polo, M.M. Abdel daiem, R. Ocampo-Pérez, Appl. Catal. B Environ. 126 (2012) 100–107.
[2] I. Velo-Gala, J.J. López-Peñalver, M. Sánchez-Polo, J. Rivera-Utrilla, Appl. Catal. B Environ. 142 (2013) 694–704.
[3] S. Ahmed, M.G. Rasul, R. Brown, M.A. Hashib, J. Environ. Manag. 92 (2011) 311–330.
[4] C.M. Teh, A.R. Mohamed, J. Alloy. Compd. 509 (2011) 1648–1660.
[5] A.Y. Shan, T.I.M. Ghazi, S.A. Rashid, Appl. Catal. A Gen. 389 (2010) 1–8.
[6] C.A. Leon, L.R. Radovic, in: P.A. Thrower (Ed.), Chemistry and Physics of Carbon, 24, Marcel Dekker, New York, 1994, pp. 213–310.
[7] T.T. Lim, P.S. Yap, M. Srinivasan, A.G. Fane, Crit. Rev. Env. Sci. Tec. 41 (2011) 1173–1230.
[8] G. Li Puma, A. Bono, D. Krishnaiah, J.G. Collin, J. Hazard. Mater. 157 (2008) 209–219.
[9] T. Cordero, C. Duchamp, J.M. Chovelon, C. Ferronato, J. Matos, J. Photochem. Photobiol. A 191 (2007) 122–131.
[10] M.H. Baek, W.C. Jung, J.W. Yoon, J.S. Hong, Y.S. Lee, J.K. Suh, J. Ind. Eng. Chem. 19 (2013) 469–477.
[11] B. Tryba, A.W. Morawski, M. Inagaki, Appl. Catal. B Environ. 41 (2003) 427–433.
[12] M. Toyoda, Y. Nanbu, T. Kito, M. Hirano, M. Inagaki, Desalination 159 (2003) 273–282.
[13] R. Leary, A. Westwood, Carbon 49 (2011) 741–772.
[14] R.W. Pekala, J. Mater. Sci. 24 (1989) 3221–3227.
[15] R.W. Pekala, C.T. Alviso, J.D. Lemey, J. Non-Cryst. Solids 125 (1990) 37–75.
[16] C. Moreno-Castilla, F.J. Maldonado-Hódar, J. Rivera-Utrilla, E. Rodríguez-Castellón, Appl. Catal. A Gen. 183 (1999) 345–356.
[17] C. Moreno-Castilla, F.J. Maldonado-Hódar, Carbon 43 (2005) 455–465.
[18] H. Rotter, V. Landau, M. Carrera, D. Goldfarb, M. Herskowitz, Appl. Catal. B Environ. 47 (2004) 111–126.
[19] M. Sánchez-Polo, J. Rivera-Utrilla, Appl. Catal. B Environ. 69 (2006) 93–100.
[20] T. Oesterreich, U. Klaus, M. Volk, B. Neidhart, M. Spiteller, Chemosphere 38 (1999) 379–392.
[21] C. Catastini, S. Rafqah, G. Mailhot, M. Sarakha, J. Photochem. Photobiol. A 162 (2004) 97–103.
[22] A. Da Pozzo, C. Merli, I. Sirés, J.A. Garrido, R.M. Rodríguez, E. Brillas, Environ. Chem. Lett. 3 (2005) 7–11.
[23] M.A. Fontecha-Cámara, M.V. López-Ramón, L.M. Pastrana-Martínez, C. Moreno-Castilla, J. Hazard. Mater. 156 (2008) 472–477.
[24] T. Mugadza, T. Nyokong, Electrochim. Acta 55 (2010) 2606–2613.
[25] N. Watanabe, S. Horikoshi, A. Kawasaki, H. Hidaka, Environ. Sci. Technol. 39 (2005) 2320–2326.
[26] J. Andersen, M. Pelaez, L. Guay, Z. Zhang, K.N. O'shea, D.D. Dionysiou, J. Hazard. Mater. 260 (2013) 569–575.
[27] F. Orellana-García, M.A. Álvarez, M.V. López-Ramón, J. Rivera-Utrilla, M. Sánchez-Polo, Chem. Eng. J. 267 (2015) 182–190.
[28] J. Rivera-Utrilla, M. Sánchez-Polo, Langmuir 20 (2004) 9217–9222.
[29] C. Moreno-Castilla, M.A. Álvarez-Merino, M.V. López-Ramón, J. Rivera-Utrilla, Langmuir 20 (2004) 8142–8148.
[30] S. Canonica, L. Meunier, U. von Gunten, Water Res. 42 (2008) 121–128.
[31] J. Rabani, W.A. Mulac, M.S. Matheson, J. Phys. Chem. 69 (1965) 53–70.
[32] C. Moreno-Castilla, F.J. Maldonado-Hódar, A.F. Pérez-Cadenas, Langmuir 19 (2003) 5650–5655.
[33] N. Job, R. Pirard, J. Marien, J.P. Pirard, Carbon 42 (2004) 3217–3227.

[34] S. Morales-Torres, F.J. Maldonado-Hódar, A.F. Pérez-Cadenas, F. Carrasco-Marín, Phys. Chem. Chem. Phys. 12 (2010) 10365–10372.
[35] N. Job, A. Théry, R. Pirard, J. Marien, L. Kocon, J.N. Rouzaud, F. Béguin, J.P. Pirard, Carbon 43 (2005) 2481–2494.
[36] O. Czakkel, K. Marthi, E. Geissler, K. László, Micropor. Mesopor. Mater. 86 (2005) 124–133.
[37] U. Zielke, J. Huttinger, W.P. Hoffman, Carbon 34 (1996) 983–998.
[38] P. Kubelka, J. Opt. Soc. Am. 38 (1948) 448–457.
[39] P. Kubelka, F. Munk, Einbeitragzuroptik der farbanstriche, Z. Tech. Phys. (Leipzig) 12 (1931) 593–601.
[40] R. López, R. Gómez, J. Sol–Gel Sci. Technol. 61 (2012) 1–7.
[41] T.S. Chen, S.E. Chiou, S.T. Shiue, Thin Solid Films 528 (2013) 86–92.

[42] G.H. Chan, B. Deng, M. Bertoni, J.R. Ireland, M.C. Hersan, T.O. Mason, R.P. Van Duyne, J.A. Ibers, Inorg. Chem. 45 (2006) 8264–8272.
[43] K.Z. Milowska, J.A. Majewski, J. Chem. Phys. 138 (2013) 194704–194714.
[44] H. Tamon, M. Okazaki, J. Colloid Interface Sci. 179 (1996) 181–187.
[45] A.B. Sifontes, M. Rosales, F.J. Méndez, O. Oviedo, T. Zoltan, J. Nanomater. 2013 (2013) 1–9.
[46] Y. Wang, R. Zhang, J. Li, L. Li, S. Lin, Nanoscale Res. Lett. 9 (46) (2014) 1–8.
[47] D. Singh, N. Singh, S.D. Sharma, C. Kant, C.P. Sharma, R.R. Pandey, K.K. Saini, J. Sol–Gel Sci. Technol. 58 (2011) 269–276.
[48] J. Matos, M. Hofman, R. Pietrzak, Carbon 54 (2013) 460–471.
[49] L. Gu, Z. Chen, C. Sun, B. Wei, X. Yu, Desalination 263 (2010) 107–112.
[50] H.P. Boehm, Carbon 50 (2012) 3154–3157.